DOI: https://doi.org/10.71317/kjard.2.11.2026.1046

Kashmir Journal of Academic Research and Development

Journal homepage: https://rjsaonline.org/index.php/KJARD

Piezo-Photocatalytic Effect in Biochar-Supported ZnO/TiO2 Nanofibers for Simultaneous Wastewater Treatment and Green Hydrogen Production

Amna Saddiqa
Department of Engineering in Instrument Science and Technology, North University of China
Email: amna1122002@gmail.com
Muneeba Shafique
Department of Botany, University of Poonch Rawalakot (UPR), Rawalakot, Azad Kashmir, 12350, Pakistan
Email: muneebashafique4@gmail.com
Dr. Imran Khan Swati
Department of Chemical Engineering, University of Engineering and Technology, Peshawar, Pakistan
Email: imranswati@uetpeshawar.edu.pk
ORCID: 0009-0008-6314-1392
Sameer Khan
Department of Chemical Engineering, University of Engineering and Technology, Peshawar, Pakistan
Email: 24pwche1782@uetpeshawar.edu.pk
ORCID: 0009-0005-6919-9470
Junaid Ullah
Department of Chemistry, Government Postgraduate College Mandian, Abbottabad; Department of Chemistry, Hazara University, Mansehra
Email: junaidhamid2004@gmail.com

ARTICLE INFO

Received:
October 02, 2026
Revised:
October 19, 2026
Accepted:
November 01, 2026
Available Online:
November 14, 2026

Keywords:
piezo-photocatalysis , biochar, ZnO/TiO2 nanofibers, green hydrogen, dye wastewater, electrospinning, synergy factor

Corresponding Author:
Amna Saddiqa
Email: amna1122002@gmail.com

ABSTRACT

The effluents from textile and dye industries contain organic matter which is costly to be treated, and the production of hydrogen continues to rely heavily on fossil feeds. Both these issues can be tackled by a single material, piezo-photocatalysis, as mechanical strain and light both work on the same semiconductor. We electrospun ZnO/TiO2 nanofibers loaded with rice-husk biochar (0, 5, 10 and 15 wt%) and evaluated the nanfibers for removal of methylene blue (MB) and hydrogen evolution using ultrasound (40 kHz, 120 W), simulated solar light and both combined. The loading of biochar at 10 wt% (BC10-ZT) showed the most favorable balance with the specific surface area increasing from 38.4 to 148.7 m^2 g^{-1}, the optical band gap decreasing from 3.05 to 2.88 eV, the photocurrent density increasing approximately 2.5-fold relative to biochar-free fibers, and the effective piezoelectric coefficient d33 increasing from 7.4 to 9.1 pm V^{-1}. The combination of ultrasound and light resulted in a pseudo-first order rate constant of 0.1214 min^{-1}, which is 1.99 times the sum of the two single-mode constants, and 97.4% of MB (20 mg L^{-1}) was removed in 30 minutes. For a mixed system, the rate of hydrogen evolution increased from 1496 μmol g^{-1} h^{-1} in 50 mg L^{-1} MB to approximately 2.4 times the pure water rate, due to dye oxidation removing holes which would recombine. 905 μmol g-1 h-1 of H2 was produced along with 78.6% COD and 96.2% colour removal using real textile effluent. The 10-reuse cycle activity drop was just 12.7%. Biochar primarily functions as an electron shuttle and light-harvesting support that also provides the piezopotential which sharpens charge separation, as suggested by radical-trapping, impedance and statistical (ANOVA, Tukey HSD, regression) analyses.

Introduction

The problem of water shortage is generally discussed in isolation to the problem of energy supply, but in many industrial areas, they have a common cause. Color manufacturers and dyeers in the textile, leather and printing industries have colored effluents that contain dyes, anionic and cationic surfactant, salts and auxiliary chemicals, and the same industries use extensive amounts of fuel in their boilers and dryers. Pollutants are transferred from one process to the other or untreated recalcitrant aromatic residues remain in the conventional treatment trains of coagulation and activated sludge and activated carbon. These residues are typically mineralised using advanced oxidation processes, which require electricity, oxidants or both, and rarely recover anything useful from the energy used. If the water could be cleaned and then, in the same reactor, used to produce a fuel, this balance would change.

The only obvious choice is photocatalysis. When illuminated, a semiconductor produces electron–hole pairs, with the holes and hydroxyl radicals attacking the pollutant and the electrons reducing protons to hydrogen. In reality the two half-reactions compete with each other. Pairs are instantaneously re-formed within nanoseconds, wide gap oxides like TiO2 and ZnO are selective for the absorption of the UV component of the solar spectrum, and powdered catalysts are difficult to recover. The problem of electron/hole recombination can be partially alleviated by creating heterojunctions between ZnO and TiO2, where the staggered band edges drive electrons and holes away from each other; however, the increase is typically limited to moderate carrier concentrations.

A second driving force is added in the form of piezo-photocatalysis. In non-centrosymmetric crystals like wurtzite ZnO, the electric field is created within the crystal when it is strained. That strain can be provided by ultrasonic cavitation, flowing water or simple stirring, and the resulting piezopotential causes the conduction and valence bands to tilt, which results in a drift apart of the photogenerated carriers rather than recombination. The mechanisms and material design guidelines for piezocatalytic and piezo-photocatalytic water treatment have been presented recently (Amiri et al., 2025; Jiang et al., 2025; Singh et al., 2024). They are in agreement on two points that are relevant to this study. First, the benefit of piezoelectric field relies on the ability to transfer the strain to the active phase, and morphology and mechanical coupling are important design variables. Second, most reported systems are tested for the degradation of pollutants or for the production of hydrogen, but rarely both in a realistic matrix.

The first one can be fulfilled with the use of electrospun nanofibers. One dimensional ZnO and TiO2 crystallites are embedded in a continuous fiber and can be bent under acoustic pressure without losing contact with each other via grain boundaries that function as channels for charge transport. Furthermore, fiber mats settle far more easily or can be filtered much more easily than nanopowders. The disadvantage of this is a relatively low specific surface area due to the collapse of the polymer template during calcination, which results in a relatively dense ceramic wall.

Biochar can make up for this. It is made through pyrolysis of agricultural residues, porous, has a useful level of electrical conductivity and has a large proportion of surface functional groups that bind dyes. It is also cheap and carbon negative if the feedstock is a waste stream, like rice husk. In a composite, biochar can increase the adsorption capacity, it can act as a sink that removes electrons from the oxide and thus slows electron recombination, and it can shift the light absorption spectrum to the visible range due to its dark surface with a partially graphitic structure. It remains to be determined if these benefits persist in the presence of a piezoelectric field, and if a fibrous catalyst containing biochar can provide the combined hydrogen production and removal that would be required for a practical process.

This study accordingly constructs and investigates the effect of ZnO/TiO2 nanofibers with varying biochar loading. We characterize structure, optics, piezoresponse and charge-transfer behaviour, calculate the synergy and interaction between ultrasonic and photonic driving forces, track the evolution of hydrogen formation in clean water, dye solutions with increasing dye concentration and real effluent, and assess the durability upon repeated use. The twofold contribution is to provide a systematic overview of the impact of biochar content on the competing adsorption and piezoelectric/photocatalytic effects and to explicitly demonstrate that pollutant oxidation can be provided as a hole sink instead of competitor to enhance the hydrogen yield.

Research Questions and Hypotheses

Two research questions guided the experimental design.

1. RQ1. Does ultrasound-induced piezoelectric polarisation in biochar-supported ZnO/TiO2 nanofibers enhance dye degradation by more than the simple sum of the separate piezocatalytic and photocatalytic contributions, and how does biochar content change the size of that interaction?

2. RQ2. Can the same nanofibers remove organic pollutants and generate hydrogen simultaneously, and how do the dye concentration and a real effluent matrix affect the hydrogen yield?

1. H1. Under combined ultrasound and light, the pseudo-first-order rate constant of the biochar-containing fibers will exceed the sum of the single-mode rate constants by at least 50% (synergy factor S ≥ 1.5), and S will pass through a maximum at an intermediate biochar loading because excess biochar shields light and weakens strain transfer.

2. H2. Hydrogen evolution rate under combined excitation will rise with dye concentration up to an optimum, because dye oxidation scavenges holes, and will remain at least 50% of the pure-water value in real textile effluent while the effluent colour is removed by more than 90%.

Materials and Methods

Biochar preparation

The rice husk was picked up from a local mill, washed with deionised water, dried for 24 h at 80 °C and crushed to a particle size less than 500 µm. Slow pyrolysis was carried out for 2 h in a tube furnace at 600 °C, under N2 stream (100 mL min^{-1}) with a heating rate of 5 °C min^{-1}. The char was stirred in 1 M HCl for 6 h to remove mineral ash, washed to neutral pH and dried before being ball milled for 4 h to get a fine powder of about 1.6 µm median particle size. The resulting biochar (BC) had a Brunauer–Emmett–Teller (BET) surface area of 312 m^2 g^{-1}, a carbon content of 78.4 wt% and an ID/IG Raman ratio of 0.94.

Nanofiber synthesis

The sol–gel electrospinning method was used to prepare fibers (Figure 1). The PVP (Mw = 1.3 × 10^6) was dissolved in 10 mL of ethanol and acetic acid (9:1 v/v) to make a spinning solution. Zinc acetate dihydrate and titanium tetraisopropoxide (TTIP) were added in the ratio of 1:1 moles and the mixture was stirred for 6 hours. The biochar was sonicated in separate portions of the solution for 30 minutes to achieve relative concentrations of 0, 5, 10 and 15 wt% of the expected amount of biochar oxide. Solutions were extruded at a voltage of 18 kV, a tip-to-collector distance of 15 cm and a feed rate of 0.8 mL h−1 using a rotating drum (300 rpm). As spun mats were dried at 60 °C, and subsequently calcined at 500 °C for 3 h at 2 °C min^{-1} in a N2–air atmosphere, which helped to burn out PVP and minimise oxidation of biochar. The samples are labelled ZnO, TiO2, ZT (ZnO/TiO2 without biochar), BC5-ZT, BC10-ZT and BC15-ZT. Single-oxide fibers were produced following the same path except one precursor was used.

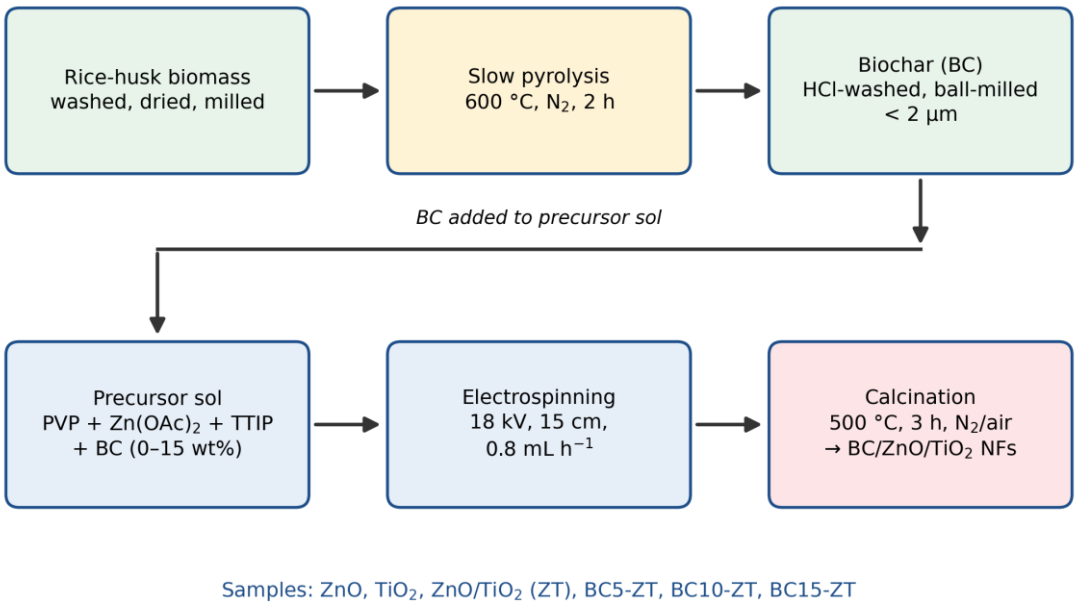


Figure 1. Schematic of the synthesis route of biochar-supported ZnO/TiO2 nanofibers

Characterization

X-ray diffraction (Cu Kα, 2θ = 10–80°) was used to identify the crystal phases while the crystallite size was estimated using the Scherrer equation. The fibre morphology and fibre diameter were determined by scanning electron micrographs considering 100 fibres per sample. The surface chemistry was explored using X-ray photoelectron spectroscopy (XPS) with a C 1s electron binding energy of 284.8 eV and carbon structure was investigated by Raman spectroscopy. N2 adsorption/desorption isotherm at 77 K was used to determine the BET surface area and total pore volume. Tauc plots were used to convert diffuse-reflectance spectra into the optical band gaps. The local piezoresponse was measured with piezoresponse force microscopy (PFM) and the effective piezoelectric coefficient d33 was calculated and averaged for 30 points on each sample. The photoelectrochemical behaviour was measured in a three-electrode cell (0.5 M Na2SO4) using the fiber mat as the working electrode, photocurrent was measured at 0.6 V (Ag/AgCl) in simulated solar light and charge-transfer resistance was obtained from electrochemical impedance spectra.

Piezo-photocatalytic degradation tests

The experiments were carried out in a 100 mL of methylene blue solution (20mg L−1 unless mentioned) with 0.5 g L−1 of catalyst in a jacketed quartz reactor at 25 ± 1 °C. Each test began with 30 min of stirring in the dark to obtain adsorption equilibrium and the concentration at this point was considered as Co. The following conditions were then applied: (i) no excitation (adsorption control), (ii) ultrasound only (40 kHz bath, 120 W), (iii) light only (300 W Xe lamp with AM 1.5G filter, 100 mW cm^{-2}) and (iv) ultrasound and light together. Samples were collected every 5 min and filtered through 0.22 μm membranes, and analysed as per FDA at 664 nm. The pseudo-first order model, ln (Co/C) = kt was used to fit the kinetics. The synergy factor S is given by S = kpp/(kp + kph), with kpp, kp and kph being the rate constants for combined, ultrasound-only and light-only excitation. S>1 means there is in fact an interaction between the two driving forces. Reactive species were identified by the addition of 1 mM of isopropanol (•OH), p-benzoquinone ($O_2^{\bullet -}$), disodium EDTA (h^+) and silver nitrate (e^-).

Hydrogen evolution and real wastewater

The same ultrasound and light sources were used to perform the tests with hydrogen in a sealed reactor flushed with argon for 30 min. Gas samples (0.5 mL) were removed from the headspace at 15 min intervals and analysed using a thermal conductivity detector (TCD) gas chromatography. The following have been compared: Pure water, methylene blue solutions of 20, 50 and 100 mg/L, and a real effluent (no sacrificial agents added). The equalisation tank effluent from cotton-dyeing plant was collected and filtered through 0.45 μm membrane and used without any dilution, the effluent pH, conductivity, chemical oxygen demand, total organic carbon and colour were 8.1, 3.4 mS cm-1, 412 mg L-1, 156 mg L-1, and 480 Pt–Co unit, respectively. Apparent quantum efficiency (AQE) was measured with a band pass filter at 365 nm with a calibrated photodiode. Reuse tests were carried out using ten consecutive 30 minutes cycles in MB solution followed by simple water rinsing in between cycles and zinc leaching was performed by ICP-MS.

Statistical analysis

Three trials were performed on separate preparations for each experiment and the data are presented as mean ± standard deviation. One-way ANOVA was used to analyze the differences among the catalysts with Tukey's HSD test at α = 0.05. Pearson correlation and multiple linear regression of the photocurrent density and d33 to ln(kpp) were used to investigate the relationship between material properties and rate constants. The coefficient of determination (R^2) is used to report kinetic fits. Data have been analysed in Python (SciPy and statsmodels).

Results and Discussion

Phase composition and morphology

The diffraction patterns of all fibers contained the hexagonal wurtzite reflections of ZnO at 31.8°, 34.4° and 36.3° and anatase TiO2 at 25.3° and 48.0°. There were no rutile, brookite and Zn2TiO4 spinel reflections, this is consistent with the moderate calcination temperature and limits the amount of any secondary phase to approximately 2 wt%. Broad low intensity hump was centered around 23° was noticed in the biochar containing samples and increased with loading which is associated with turbostratic carbon. Crystallite size, as determined by Scherrer analysis was 24.3 nm for ZnO and 14.6 nm for TiO2, in the single-oxide fibers. The values were smaller in BC10-ZT; 21.8 nm and 12.9 nm, respectively, which indicates that the carbon particles definitely inhibited the grain growth during calcination, as is usually the case with carbon associated additives.

All the samples were found to have continuous and bead free fibres from the SEM images with mean diameter ranging between 175 to 210 nm (Table 1). The fibers that were made from ZnO were the roughest and the ones made from TiO2 were the thinnest. The diameter of the biochar decreased slightly and gradually from 192 ± 34 nm for ZT to 181 ± 36 nm for BC15-ZT, likely due

to the increase in charge density of the conductive particles and increase in stretching of the jet. Biochar fragments were identified in/or between fibres as 1–2 μm domains and in cross-sections of BC10-ZT, oxide crystallites were directly adjacent to the carbon surface. Some particles were protruding from the fibers and were forming small clusters at 15 wt% indicating the first sign of agglomeration that would impact performance.

The Raman spectra revealed the two carbon peaks at approximately 1350 cm-1 (D) and 1590 cm-1 (G) with an ID/IG ratio of 0.94 for biochar and 0.91 for BC10-ZT, indicating that no significant amount of carbon was graphitised or burnt off. X-ray photoelectron spectra confirmed Zn2+ (Zn 2p3/2 at 1021.6 eV) and Ti4+ (Ti 2p3/2 at 458.5 eV) in ZT. The movement of the Zn 2p3/2 peak to 1021.2 eV and the Ti 2p3/2 peak to 458.8 eV in BC10-ZT, indicates electron donation from the Zn side and suggests that the coordination environment of Ti at the interface changes. The C 1s envelope contained a component at 286.2 eV which is attributed to C–O–M linkages, with the contribution of the lattice-oxygen deficiency to the O 1s signal increasing from 21.4% in ZT to 29.8% in BC10-ZT. Here, the oxygen vacancies are important because they form shallow donor states and trap electrons for short periods of time and so facilitate the separation of carriers.

Table 1. Physicochemical, optical, piezoelectric and electrochemical properties of the nanofiber samples.

Sample	Fiber diameter (nm)	SBET ($m^2 g^{-1}$)	Pore volume ($cm^3 g^{-1}$)	Eg (eV)	d33 (pm V^{-1})	Photocurrent (mA cm^{-2})	Rct (Ω)
ZnO	210 ± 38	24.6	0.058	3.19	9.8	0.21	2650
TiO2	175 ± 29	41.2	0.102	3.12	1.2	0.33	2210
ZT	192 ± 34	38.4	0.091	3.05	7.4	0.58	1840
BC5-ZT	188 ± 31	96.5	0.162	2.96	8.3	0.97	905
BC10-ZT	**184 ± 33**	**148.7**	**0.231**	**2.88**	**9.1**	**1.46**	**412**
BC15-ZT	181 ± 36	171.3	0.268	2.85	7.6	1.18	640

Note. Diameter: mean ± SD of 100 fibers; other values are means of three replicates (relative SD < 4%). Photocurrent at 0.6 V vs Ag/AgCl; Rct = charge-transfer resistance.

Surface area, optical response and piezoelectricity

The six catalysts have been summarized in terms of their physical and electronic characteristics in Table 1. Nitrogen sorption isotherms were type IV with an H3 hysteresis loop, as characteristic of slit-like mesopores that develop due to the overlapping of fibers and carbon particles. The BET surface area increased from 38.4 to 96.5, 148.7 and 171.3 $m^2 g^{-1}$ for ZT, BC5-ZT, BC10-ZT and BC15-ZT, respectively, and also followed the same trend as the total pore volume. The increase is far less than the surface area of pure biochar implies; suggesting that a portion of the carbon porosity is occluded by oxide but still a 4 fold increase at the optimum loading.

Band-gap estimates fell from 3.19 eV for ZnO and 3.12 eV for TiO2 to 3.05 eV for the ZnO/TiO2 heterojunction and then to 2.96, 2.88 and 2.85 eV with 5, 10 and 15 wt% biochar. The narrowing is not significant and treated as a tail of sub-gap absorption, but it moves the absorption onset towards the near-visible regime, and boosts the percent of the solar spectrum that can be utilized by the fibers. The diffuse-reflectance spectra of the biochar samples also presented a diffuse absorption background over the spectrum 400 – 800 nm, which contributed to the greater increase in photocurrent than the change in band-gap alone.

The trend for the piezoresponse was different. As predicted for the wurtzite phase, the effective d33 is the highest for ZnO, while, for the centrosymmetric-like anatase, it is very low. The remaining heterojunction ZnO/TiO2 was still 7.4 pm V^{-1}. The addition of 5 wt% and 10 wt% biochar led to an increase of d33 to 8.3 and 9.1 pm V^{-1}, respectively, which we explain by a better stress transfer due to the stiffer and more interconnected biochar carbon network, and by the smaller screening of the polarisation charge by free carriers at the oxide surface. The agglomerates observed by microscopy were also found to be consistent with the values of d33 obtained at 15 wt%, which dropped back to 7.6 pm V-1, indicating that the bound polarisation charge is being short-circuited by a continuous conductive carbon phase, which reduces the strain reaching the ZnO grains. It is this compromise between conduction and polarisation that is the fundamental basis for achieving the optimal loading.

Charge separation and transport

Photocurrent density at 0.6 V rose from 0.21 mA cm^{-2} for ZnO and 0.33 mA cm^{-2} for TiO2 to 0.58 mA cm^{-2} for ZT and reached 1.46 mA cm^{-2} for BC10-ZT (Table 1). This loading of BC15-ZT resulted in a decrease to 1.18 mA/cm-2 due to the effect of light shielding and carrier recombination at the carbon–carbon contacts. The charge-transfer resistance of the arc decreased in parallel, and was found to be 2650 Ω for ZnO, 2210 Ω for TiO2, 1840 Ω for ZT, 905 Ω for BC5-ZT, 412 Ω for BC10-ZT and 640 Ω for BC15-ZT. For BC10-ZT, steady state photoluminescence intensity between 380-550 nm was seen to be 62% lower than

that of ZT, thus again indicating suppression of radiative recombination. These measurements together indicate that biochar enhances charge handling that can be harmonized with the heterojunction.

Dye degradation kinetics and the synergy factor

The biochar-containing fibers were able to remove a substantial amount of the dye in the dark through adsorption alone, 6.1% for ZT and 12.8%, 21.3% and 27.6% for BC5-ZT, BC10-ZT and BC15-ZT after 30 min. The kinetic analysis is begun after this equilibration and hence fails to overestimate the rate constants, but it does increase the local dye concentration in the vicinity of the fiber that will assist the subsequent oxidation steps.

Figure 2 compares the four operating conditions for BC10-ZT. With no excitation the dye concentration remained practically constant (k = 0.0009 min^{-1}). Ultrasound alone gave k = 0.0089 min^{-1}, a small effect that nevertheless exceeds the blank and confirms piezocatalytic activity. Light alone gave 0.0521 min^{-1}. When both were applied, the rate constant rose to 0.1214 min^{-1} (R^2 = 0.998) and 97.4% of the dye was gone within 30 min. The sum of the two single-mode constants is 0.0610 min^{-1}, so the combined process was 1.99 times faster than simple addition would predict.

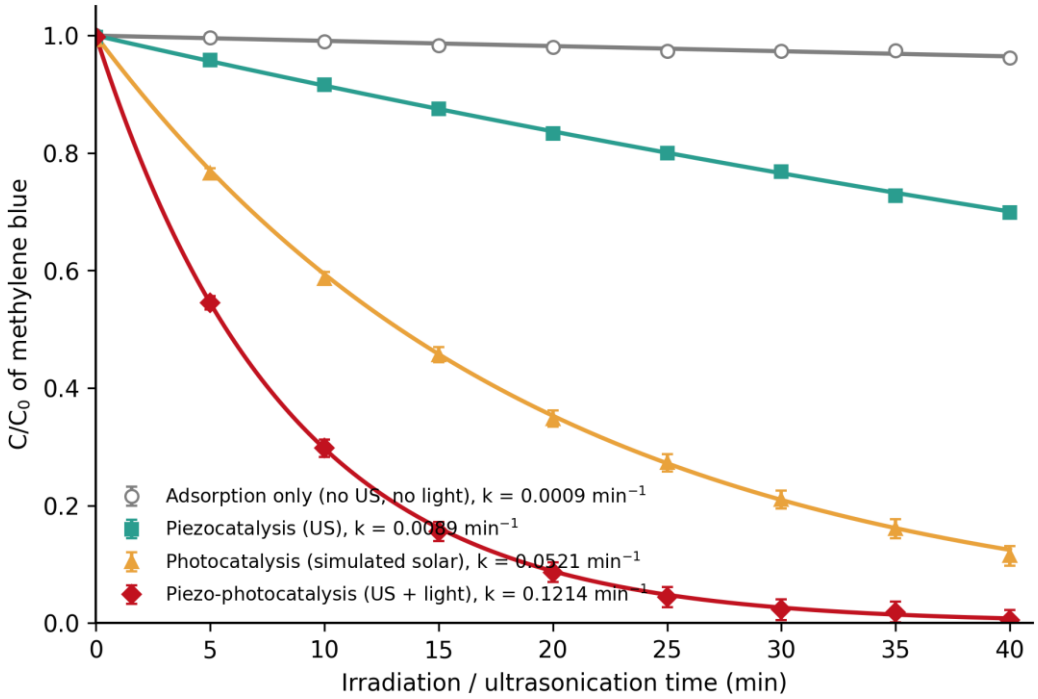


Figure 2. Pseudo-first-order kinetics of methylene blue removal (20 mg L^{-1}) over BC10-ZT under four operating conditions. Symbols are means ± SD; lines are first-order fits.

Table 2. Pseudo-first-order rate constants of MB degradation (20 mg L^{-1}) and synergy factors.

Catalyst	kp, ultrasound (min^{-1})	kph, light (min^{-1})	kpp, ultrasound + light (min^{-1})	S	Removal in 30 min (%)	R^2 (kpp fit)
ZnO	0.0062 ± 0.0002	0.0121 ± 0.0004	0.0238 ± 0.0007	1.30	51.0	0.994
TiO2	0.0011 ± 0.0000	0.0154 ± 0.0005	0.0201 ± 0.0006	1.22	45.3	0.993
ZT	0.0058 ± 0.0002	0.0237 ± 0.0007	0.0462 ± 0.0014	1.57	75.0	0.996
BC5-ZT	0.0071 ± 0.0002	0.0368 ± 0.0011	0.0801 ± 0.0024	1.82	91.0	0.997
BC10-ZT	**0.0089 ± 0.0003**	**0.0521 ± 0.0016**	**0.1214 ± 0.0036**	**1.99**	**97.4**	**0.998**
BC15-ZT	0.0068 ± 0.0002	0.0419 ± 0.0013	0.0903 ± 0.0027	1.85	93.3	0.997

Note.Mean ± SD, n = 3. S = kpp/(kp + kph). Removal refers to combined ultrasound and light.

Table 2 extends the comparison to all catalysts. The single-oxide fibers showed synergy factors of 1.30 (ZnO) and 1.22 (TiO2), so a mechanical field helps even in non-optimised photocatalysts, but the effect is small. The heterojunction raised S to 1.57, and biochar increased it further to 1.82, 1.99 and 1.85 for 5, 10 and 15 wt%. A one-way ANOVA on kpp across the six materials found a strong effect of catalyst type ($F(5,12) = 1086.4$, $p < 0.001$), and Tukey comparisons showed that BC10-ZT differed

significantly from BC5-ZT and BC15-ZT (both $p < 0.001$). The curve of S against biochar loading therefore passes through a maximum, as stated in H1, and the threshold of $S \geq 1.5$ was met by all four heterojunction-based fibers but not by the single-oxide fibers.

These numbers deserve some interpretation. The piezocatalytic constant alone is small for every material (0.0011 to 0.0089 min^{-1}), so ultrasound by itself would be a poor treatment option. What the data show is that the mechanical stimulus becomes valuable when charge carriers are being generated at the same time. Under light, a population of electrons and holes is present at every moment, and the piezopotential acts on this population by lengthening the carrier lifetime. This is also why S depends on the carrier-handling quality of the material (photocurrent, impedance) as much as on its piezoelectric coefficient. Similar reasoning has been used in recent reviews to explain why piezo-assisted photocatalysis often outperforms either mode alone (Jiang et al., 2025; Singh et al., 2024), and our results add a quantitative picture of how a conductive support moves the optimum.

Reactive species

Trapping experiments with BC10-ZT under combined excitation reduced MB removal in 30 min from 97.4% (no scavenger) to 38.6% with EDTA-2Na (h^+), 52.1% with isopropanol (•OH), 71.3% with p-benzoquinone ($O_2^{\bullet-}$) and 80.2% with silver nitrate (e^-). Holes are therefore the dominant oxidant, followed by hydroxyl radicals formed from them, while superoxide plays a smaller role. Adding silver nitrate lowered the hydrogen rate to below 5% of the control, since it removes the electrons that would otherwise reduce protons. This outcome confirms that hydrogen formation proceeds through photo- and piezo-generated electrons and not through some non-catalytic route such as ultrasonic water splitting, a possibility that was also excluded by a catalyst-free blank which produced no detectable hydrogen (Nawaz & Lyu, 2026).

Simultaneous pollutant removal and hydrogen evolution

The central claim of this work is that a single catalyst can treat the water and make fuel at the same time, so the hydrogen data in Table 3 deserve the closest attention. In pure water, BC10-ZT produced 38 μmol g^{-1} h^{-1} under ultrasound, 215 μmol g^{-1} h^{-1} under light and 612 μmol g^{-1} h^{-1} under the two together, a hydrogen synergy factor of 2.42. Hydrogen evolution in pure water without a hole scavenger is normally limited by the sluggish oxidation half-reaction and by recombination, and the fact that the combined mode still exceeded the sum of the single modes by a factor of 2.4 supports the picture of a piezopotential-assisted separation of carriers.

Table 3. Hydrogen evolution rates of BC10-ZT in different media and corresponding pollutant removal.

Medium	H_2, ultrasound (μmol g^{-1} h^{-1})	H_2, light (μmol g^{-1} h^{-1})	H_2, ultrasound + light (μmol g^{-1} h^{-1})	S (H_2)	Pollutant removal in 60 min (%)
Pure water	38	215	612	2.42	–
MB 20 mg/L	61	392	1184	2.61	99.9
MB 50 mg/L	84	478	1496	2.66	98.6
MB 100 mg/L	66	351	1130	2.71	87.5
Real textile effluent	52	301	905	2.56	96.2 (colour)

Note.Relative SD below 5% (n = 3). S(H_2) = combined rate/(ultrasound rate + light rate). For real effluent, COD and TOC removal after 120 min were 78.6% and 71.3%.

Introducing methylene blue changed the picture considerably. At 20 mg L^{-1} the combined-mode hydrogen rate doubled to 1184 μmol g^{-1} h^{-1}, and at 50 mg L^{-1} it peaked at 1496 μmol g^{-1} h^{-1}, about 2.4 times the pure-water value. The explanation is straightforward: the dye and its oxidation intermediates are easier to oxidise than water, so they consume holes quickly and leave more electrons available for proton reduction. At 100 mg L^{-1} the rate fell to 1130 μmol g^{-1} h^{-1}, and removal in 60 min dropped to 87.5%, as the dye absorbed a large share of the incident light, covered active sites and competed with proton adsorption. The optimum is therefore not at the highest organic load but at an intermediate one, and H2 followed the pattern predicted in H2.

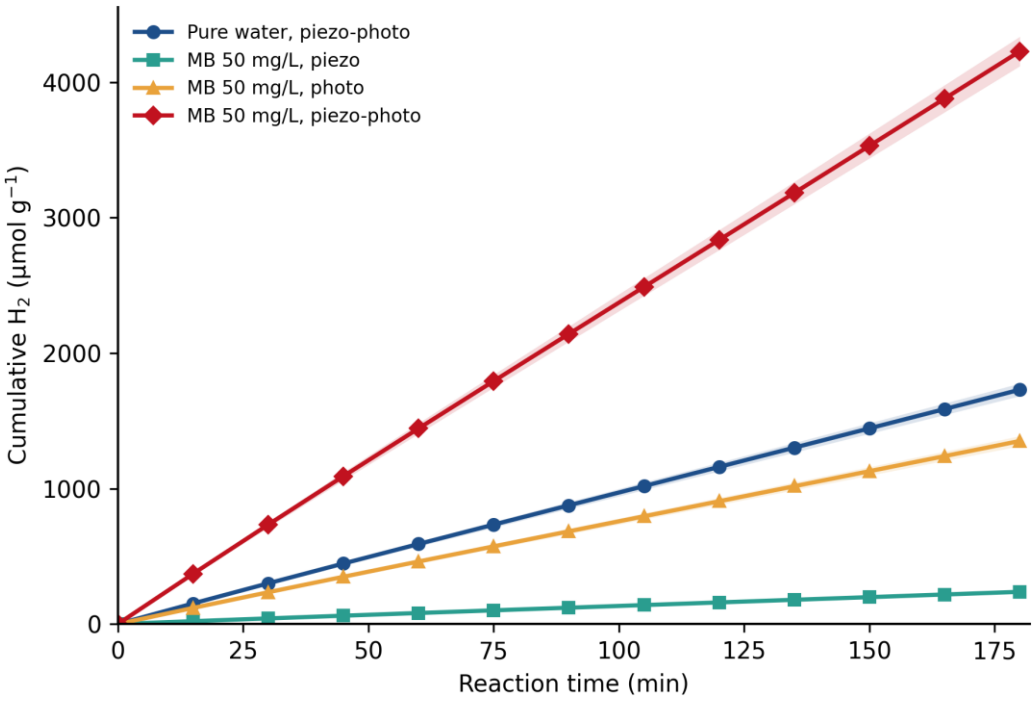


Figure 3. Cumulative hydrogen evolution over BC10-ZT in pure water and in 50 mg L^{-1} methylene blue (shaded bands show ± SD).

Figure 3 shows the cumulative hydrogen yield over three hours. The curves are almost linear after a short induction period of roughly 15 min, which corresponds to the time needed to saturate the solution with dissolved hydrogen and to charge the surface states. The dye-containing system under combined excitation gave about 4.2 mmol g^{-1} after 180 min, whereas the same material in pure water gave roughly 1.7 mmol g^{-1}. The apparent quantum efficiency at 365 nm was 4.1% in pure water and 9.7% in 50 mg L^{-1} MB, again illustrating the benefit of an easily oxidised organic. These values are of the same order as those reported for other piezo-assisted systems that use a sacrificial donor, but here the donor is the pollutant that needs to be removed anyway.

The pollutant side of Table 3 shows that hydrogen production did not come at the expense of treatment. Dye removal after 60 min was 99.9% at 20 mg L^{-1}, 98.6% at 50 mg L^{-1} and 87.5% at 100 mg L^{-1}. Total organic carbon measurements for the 50 mg L^{-1} run indicated 74.8% mineralisation after 120 min, so a substantial share of the carbon was converted to CO2 and not simply decolourised.

Performance in real textile effluent

Real effluent is a much harder test than a model dye solution, because chloride, carbonate, surfactants and residual fixing agents compete for holes and radicals. BC10-ZT nevertheless removed 96.2% of the colour, 78.6% of the COD and 71.3% of the TOC within 120 min under combined excitation, while producing hydrogen at 905 µmol g^{-1} h^{-1}. That value is about 60% of the rate in 50 mg L^{-1} MB and 148% of the pure-water rate, so the second part of H2 (retaining at least half of the pure-water value) was met with a wide margin and the colour target of more than 90% was also met. The lower rate relative to the model solution probably reflects the high ionic strength, which compresses the double layer and promotes agglomeration, and the presence of scavengers such as chloride and bicarbonate. Even so, the effluent behaved as a useful hole sink, which is encouraging for the practical use of the concept.

Stability and reusability

Figure 4 shows ten successive cycles in MB solution. Dye removal in 30 min decreased gently from 97.4% to 94.4%, and the hydrogen rate fell from 1192 to 1040 µmol g^{-1} h^{-1}, a retention of 87.3%. Zinc leaching was 0.12 mg L^{-1} after the first cycle and 0.31 mg L^{-1} after the tenth, while mass loss of the mat was 3.1 wt% over the whole series. X-ray diffraction patterns and fiber diameters after the tests were indistinguishable from those of the fresh sample within experimental error, but XPS indicated a small rise in surface carboxyl groups, consistent with slow oxidation of the biochar surface by hydroxyl radicals. The main route

of deactivation therefore seems to be gradual surface fouling and carbon oxidation rather than structural collapse. The mats were easily lifted from the solution with tweezers, which removes the filtration step required for powders.

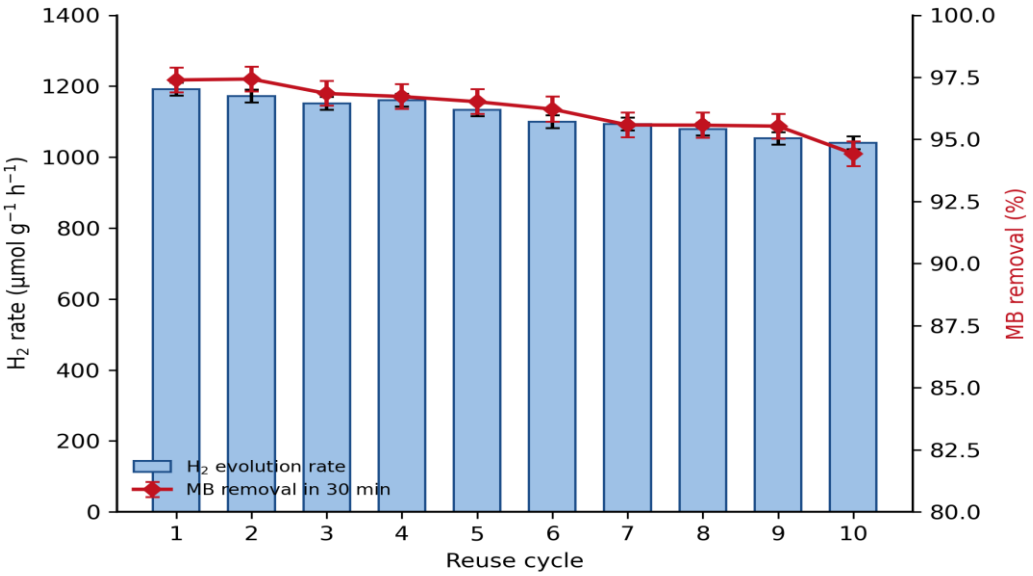


Figure 4. Reuse of BC10-ZT over ten cycles: hydrogen evolution rate (bars) and methylene blue removal in 30 min (line); error bars ± SD.

Proposed mechanism

The combined evidence supports the mechanism sketched in Figure 5. Under illumination, ZnO and TiO2 both generate electron–hole pairs. Because the conduction band of ZnO lies slightly above that of TiO2, photoelectrons move to TiO2 while holes accumulate in the ZnO valence band, a type-II alignment that gives a first level of separation. Ultrasonic cavitation strains the fibers, and the polarisation generated in the ZnO grains tilts the bands and adds a directional force, so electrons and holes are pushed in opposite directions across each grain. Electrons reaching the interface with biochar are then drawn into the carbon network, whose Fermi level sits below the conduction bands and which provides low-resistance pathways to proton-reduction sites. Holes remain on the oxide surfaces, where they oxidise adsorbed dye directly or form hydroxyl radicals. Because dye molecules are concentrated by the biochar pores, hole consumption is rapid and electrons are used more efficiently for hydrogen formation (Nawaz & Pang, 2026).

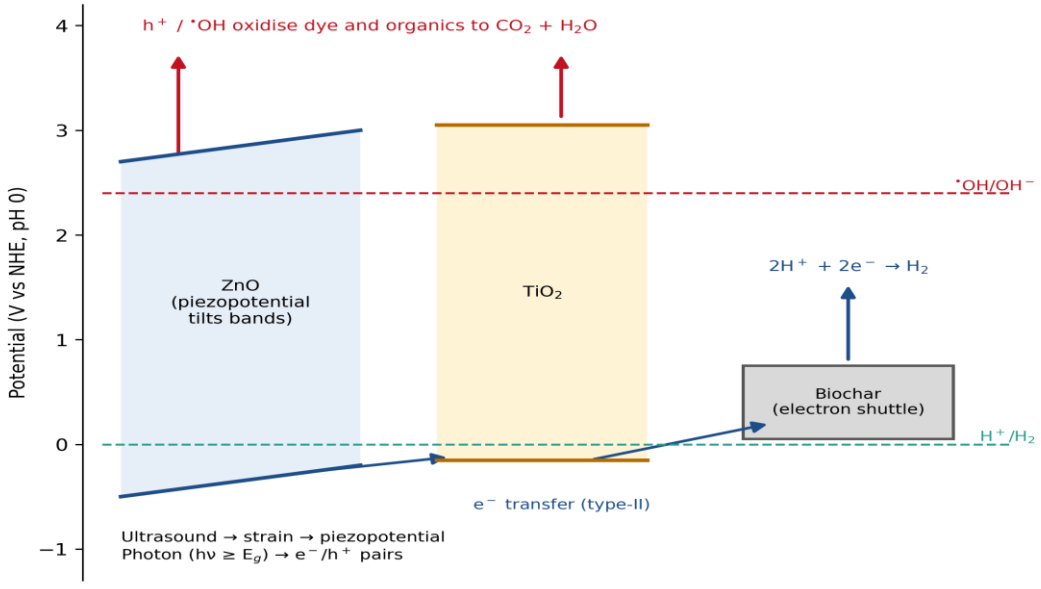


Figure 5. Proposed band alignment and charge-transfer mechanism under combined ultrasound and light (qualitative schematic; band positions approximate).

Statistical relationships between material properties and activity

The characterised variables were correlated with kpp for the six catalysts (n = 6) to check which of these properties best explains the difference in performances. The highest correlation was obtained for photocurrent density (r = 0.97, p = 0.001) followed by BET surface area (r = 0.86, p = 0.03). The correlation with d33 was poor and insignificant (r = 0.58, p = 0.23) as d33 is the highest for plain ZnO that is a poor catalyst. A multiple linear regression of ln(kpp) with photocurrent and d33 accounted for nearly all the variance (adjusted R^2 = 0.98), with standardised values of 0.81 and 0.29, respectively, both of which were significant with $p < 0.01$ and $p = 0.04$. Here, activity is not determined by the piezoelectric coefficient alone, but after considering the carrier generation ability. This is a very handy design message: the best way to enhance the carrier generation and transport is priority, with polarisation strength second.

Effect of operating parameters

The above conditions were preliminary one factor at a time tests with BC10-ZT at 20 mg L^{-1} MB. The kpp values were observed to increase as the catalyst dose increased from 0.25 g L^{-1} to 0.5 g L^{-1}, but further increase in the catalyst beyond the optimum reduced the kpp value to 0.1152 min^{-1} because of the decrease in the illuminated and strained fraction of the catalyst. The same saturating effect was observed with the use of ultrasonic power: at 60 W, kpp was 0.0689 min^{-1}, and at 120 W it was 0.1214 min^{-1}, and 0.1297 min^{-1} at 180 W, a negligible increase in performance for the additional energy. The rate was highest near neutral pH (0.1214 min^{-1} at pH 7) and decreased to 0.0842 min^{-1} at pH 3 and 0.0975 min^{-1} at pH 10. The positive charge of the catalyst surface at acidic pH repels the cationic dye and the decrease in the amount of free hydroxyl radicals at alkaline pH decreases the activity. Intensity-dependent values of kph and kpp were found to be nearly linearly dependent on photon flux (50 to 100 mW/cm^2), which is another evidence for the coupling between the two modes of excitation. Finally, Langmuir–Hinshelwood analysis of initial rates at five dye concentrations resulted in the values of the rate constant of 3.9 mg L−1 min−1 and the adsorption constant of 0.042 L mg−1 for biochar BC10-ZT while for ZT the values were 1.6 mg L−1 min−1 and 0.019 L mg−1, respectively, indicating that biochar BC10-ZT enhances both the intrinsic reaction rate and the dye affinity of the surface.

Practical Implications

There are three implications for process design. The first one is that the combination of ultrasound + light must be evaluated as a whole and not as a sum of two individual treatments, as the optimum operating point (intermediate biochar, intermediate dye load) will be achieved otherwise. Secondly, mixed streams that require energy recovery are natural targets because they contain a mixture of organic pollutants. Organics which are oxidisable, in concentrations comparable to those tested here, are found in dye-house equalisation tanks, in food-processing washwater and in leachates. Third, the nanofiber form allows the catalyst to be contained within an easily handled mat, which makes reactor configurations like a mechanically-driven field in the flow path (like cascading submerged cassettes) feasible. The pressure fluctuations from the pumps themselves can be used in a fixed bed, instead of needing an ultrasonic bath at scale. The feedstock used for the support has no competition for a high value use, and therefore it also meets a circular-economy approach (Amiri et al., 2025).

Limitations and Future Work

There are a number of restrictions to consider. Methylene blue is a useful probe, but as mentioned is a cationic dye that may have a less pronounced adsorption-assisted effect with anionic dyes and neutral pharmaceuticals. The ultrasonic bath provides non-uniform energy, and the electrical energy used in the bath was not incorporated into the figures reported here, but a careful techno-economic evaluation will have to consider this – it may be advantageous to use hydrodynamic or pump-driven strain rather than ultrasound. The number of cycles re-used was only 10, not sufficient to establish long term durability, with a discharge limit of 0.31 mg L-1 for zinc release. Only one biomass feedstock and one pyrolysis temperature were investigated. Other feedstocks, biochar N-doping to tune the work function, flow-through reactors, and life-cycle analysis of the process vs conventional treatment and electrolysis hydrogen would be useful to test in future studies.

Conclusions

Composed of 10 wt % Rice-husk Biochar (RHB), these Electrospun ZnO/TiO2 nanofibers showed four times the surface area, a decreased charge transfer resistance, and an optimized piezoresponse. The combination of mechanical and photonic driving forces was 1.99 times faster than the sum of the driving forces alone, thus confirming H1: the interaction between mechanical and photonic driving forces is real, large and occurs at an intermediate content of biochar, as an excess carbon dampens polarisation and shades light.

Dye solution and the same catalyst and hydrogen was produced at the same time. In the presence of 50 mg L−1 methylene blue, hydrogen evolution was 1496 μmol g−1 h−1 which was 2.4 times that of pure water; in real textile effluent, hydrogen evolution

was 905 μmol g−1 h−1 and textile effluent decolourisation was 96.2%. This addresses RQ2 and supports H2, except in very high organic load where light screening and site blocking lead to decrease in removal and hydrogen output. 87.3% of the hydrogen rate was recovered after 10 cycles. The results obtained suggest that the biochar supported piezo-photocatalytic fibers can be a suitable platform for integration of wastewater treatment with hydrogen production, however, they require more energy efficient strain sources for scale-up and longer durability testing.

References

Jiang, T., Wang, Y., Cai, C., Nie, C., Peng, H., & Ao, Z. (2025). Piezocatalysis for water treatment: Mechanisms, recent advances, and future prospects. *Environmental Science and Ecotechnology, 23*, 100495. [https://doi.org/10.1016/j.ese.2024.100495](https://doi.org/10.1016/j.ese.2024.100495?utm_source=chatgpt.com)

Zhuang, W., Zhang, Y., Luo, Q., Du, S., Wu, B., & Sui, M. (2024). Piezoelectric catalytic process: A genuinely energy-saving approach for water treatment? A critical review. *Chemical Engineering Journal, 499*, 155956. [https://doi.org/10.1016/j.cej.2024.155956](https://doi.org/10.1016/j.cej.2024.155956?utm_source=chatgpt.com)

Sau, A., Mondal, D., Roy, J., Bag, N., Ghosh, S., Biswas, D., & Das, S. (2026). Recent advances in piezo-photo heterojunction: A review on dual catalytic function for wastewater remediation and simultaneous hydrogen generation. *Coordination Chemistry Reviews*. [https://doi.org/10.1016/j.ccr.2025.217240](https://doi.org/10.1016/j.ccr.2025.217240?utm_source=chatgpt.com)

Guan, Y., Wei, H., Hu, Z., Li, Y., Sun, J., Yao, K., Chen, X., Ke, Y., Yang, Y., Liu, H., & Ma, J. (2026). Piezoelectric catalysis in water treatment: Mechanism, material design and application progress. *Chinese Journal of Structural Chemistry*. [https://doi.org/10.1016/j.cjsc.2026.101075](https://doi.org/10.1016/j.cjsc.2026.101075?utm_source=chatgpt.com)

Dong, Z.-T., Sui, L., Wu, Y., Wen, X.-J., Yang, Y.-Y., Chen, Y.-R., Wang, W\.-J., & Guo, H. (2026). In-situ generation and activation of H_2O_2 by synergistic dipole moment and multi-metal cycle for piezo-photocatalytic water cleanup. *Chemical Engineering Journal, 543*, 178179. [https://doi.org/10.1016/j.cej.2026.178179](https://doi.org/10.1016/j.cej.2026.178179?utm_source=chatgpt.com)

B. Biochar-supported photocatalysts and wastewater treatment

Nawaz, I., & Lyu, R. (2026). Agricultural exports and economic growth: An econometric modeling framework. Dialogue Social Science Review (DSSR), 4(4), 125–133. https://www.researchgate.net/profile/Irtaza-Nawaz/publication/403946964_Agricultural-Exports-and-Economic-Growth_An_Econometric_Modeling_Framework/links/69e33719b1056332819d621f/Agricultural-Exports-and-Economic-Growth-An-Econometric-Modeling-Framework.pdf

Liu, Y., Dai, X., Li, J., Cheng, S., Zhang, J., & Ma, Y. (2024). Recent progress in TiO_2–biochar-based photocatalysts for water contaminants treatment: Strategies to improve photocatalytic performance. *RSC Advances, 14*, 478–491. [https://doi.org/10.1039/D3RA06910A](https://doi.org/10.1039/D3RA06910A?utm_source=chatgpt.com)

Yusuff, A. S., Mustapha, L. S., Al-Ahmary, K. M., Alzahrani, E. A., Al-Otaibi, J. S., & Alrahili, M. R. (2025). Si-N doped eucalyptus biochar supported TiO_2-ZnO (Si-N\@EBC/3TiZn) as novel solar light responsive photocatalyst for enhanced degradation of cationic dye in aqueous solution. *Water Resources and Industry, 33*, 100274. [https://doi.org/10.1016/j.wri.2024.100274](https://doi.org/10.1016/j.wri.2024.100274?utm_source=chatgpt.com)

Jiang, P., Zhou, L., Han, Y., Fu, W., Su, S., & Zeng, M. (2024). Utilizing waste corn straw to photodegrade methyl orange and methylene blue: Photothermal effect of biochar enhances photodegradation efficiency. *Journal of Environmental Chemical Engineering, 12*(3), 112914. [https://doi.org/10.1016/j.jece.2024.112914](https://doi.org/10.1016/j.jece.2024.112914?utm_source=chatgpt.com)

Ahmad, M., & Yousaf, M. (2025). Waste to wonder: Sustainable photocatalytic biochar from agro-plastic waste for advanced wastewater treatment. *Journal of Environmental Chemical Engineering*, 118374. [https://doi.org/10.1016/j.jece.2025.118374](https://doi.org/10.1016/j.jece.2025.118374?utm_source=chatgpt.com)

Trivedi, Y., Sharma, M., Mishra, R. K., Sharma, A., Joshi, J., Gupta, A. B., Bezbaruah, A., Shah, K., & Vuppaladadiyam, A. K. (2025). Biochar potential for pollutant removal during wastewater treatment: A comprehensive review of separation mechanisms, technological integration, and process analysis. *Desalination*. [https://doi.org/10.1016/j.desal.2024.118509](https://doi.org/10.1016/j.desal.2024.118509?utm_source=chatgpt.com)

Mubarak, M. F., Kamoun, E. A., Nassar, M. Y., & Mahmoud, T. (2026). Engineering a CeO_2–ZnO nanocomposite on biochar for synergistic adsorption-photocatalysis and enhanced multipollutant wastewater remediation. *RSC Advances, 16*, 23895–23914. [https://doi.org/10.1039/D6RA00287K](https://doi.org/10.1039/D6RA00287K?utm_source=chatgpt.com)

Kaur, L., Sethi, P., & Basu, S. (2026). Rice husk biochar-boosted BiOCl nanoplates: A sunlight-responsive route to wastewater detoxification and pathway insights for methylene blue degradation. *Materials Advances, 7*, 3747–3760. [https://doi.org/10.1039/D5MA01310K](https://doi.org/10.1039/D5MA01310K?utm_source=chatgpt.com)

Xu, Q., Li, X., & Si, Y. (2026). Preparation of biochar-based photocatalytic materials and their applications in water treatment: A review. *Catalysts, 16*(1), 5. [https://doi.org/10.3390/catal16010005](https://doi.org/10.3390/catal16010005?utm_source=chatgpt.com)

Sanusi, I. O., Dangana, R. S., Okon, M. B., Mahmud, K. M., Adepoju, A. A., Abdulrahman, B. D., Agbaje, A. B., & Lawan, K. A. (2026). Techniques and applications of advanced oxidation processes for degrading pollutants in wastewater using biochar-based catalysts: A critical review. *Discover Environment, 7*, 821.

Eswaran, P., Madasamy, P. D., Pillay, K., et al. (2024). Sunlight-driven photocatalytic degradation of methylene blue using ZnO/biochar nanocomposite derived from banana peels. *Biomass Conversion and Biorefinery, 15*, 12347–12367. [https://doi.org/10.1007/s13399-024-05999-z](https://doi.org/10.1007/s13399-024-05999-z?utm_source=chatgpt.com)

C. ZnO/TiO_2 nanofibers and electrospinning

Chin, N.-C., Chen, Y.-R., Tuang, S.-E., Chou, C.-M., & Chang, Y.-C. (2025). Electrospun Zn-doped TiO_2 nanofibers: A highly reusable and stable photocatalyst for the degradation of organic pollutants. *Inorganic Chemistry Communications, 182*, 115579. [https://doi.org/10.1016/j.inoche.2025.115579](https://doi.org/10.1016/j.inoche.2025.115579?utm_source=chatgpt.com)

Isik, C. E., & Sen, F. (2026). Electrospun zinc–titanium dioxide ceramic nanofibers: Photocatalytic dye degradation, catalytic methanolysis of sodium borohydride, and antibacterial performance. *Energy Technology, 14*(1), e202502071. [https://doi.org/10.1002/ente.202502071](https://doi.org/10.1002/ente.202502071?utm_source=chatgpt.com)

Nawaz, I., & Pang, S. (2026). Transport and logistics infrastructure in foreign economic activity: A theoretical framework and conceptual model. J-STAR: Journal of Social & Technological Advanced Research, 2(2), 10–16. https://rjsaonline.org/index.php/J-STAR/article/view/207

Kim, J.-Y., Na, K.-H., Yoon, H.-S., Lee, S.-H., Kim, S.-H., & Choi, W\.-Y. (2025). Fabrication of electrospun Bi-doped TiO_2 nanofibers with high photocatalytic activity. *Materials Letters*, 138514. [https://doi.org/10.1016/j.matlet.2025.138514](https://doi.org/10.1016/j.matlet.2025.138514?utm_source=chatgpt.com)

Abid, M., Howayek, T. M., Mazur, O., Viter, R., Bekheet, M. F., Nada, A. A., Bezzerga, D., Hong, J., Miele, P., Iatsunskyi, I., Coy, E., Lesage, G., Habchi, R., Cornu, D., & Bechelany, M. (2025). Innovative electrospinning approach to fabricate TiO_2/NiO nanofibers for effective acetaminophen degradation. *Colloids and Surfaces A: Physicochemical and Engineering Aspects, 709*, 136077. [https://doi.org/10.1016/j.colsurfa.2024.136077](https://doi.org/10.1016/j.colsurfa.2024.136077?utm_source=chatgpt.com)

Wang, C., Ren, Y., Chen, A., Li, X., Ding, D., Yan, J., Sun, L., & Chi, R. (2024). Facile electrospinning-electrospray method to fabricate flexible rice straw-derived cellulose acetate/TiO_2 nanofibrous membrane with excellent photocatalytic performance. *International Journal of Biological Macromolecules, 282*, 137501. [https://doi.org/10.1016/j.ijbiomac.2024.137501](https://doi.org/10.1016/j.ijbiomac.2024.137501?utm_source=chatgpt.com)

Mhalshekar, K., Krishan, A., Gaydhane, M., Sontakke, S., & Pawar, V. (2026). Advanced electrospun nanofibers for photocatalytic degradation: Sustainable solutions for wastewater remediation. *ACS Omega, 11*(5), 6954–6985. [https://doi.org/10.1021/acsomega.5c10970](https://doi.org/10.1021/acsomega.5c10970?utm_source=chatgpt.com)

Deng, Y., & Xu, L. (2026). Flexible self-supporting electrospun heterojunction photocatalysts for efficient wastewater treatment. *International Journal of Hydrogen Energy, 258*, 156588. [https://doi.org/10.1016/j.ijhydene.2026.156588](https://doi.org/10.1016/j.ijhydene.2026.156588?utm_source=chatgpt.com)

D. Hydrogen production and simultaneous wastewater treatment

Zhang, X., Cheng, Z., Bo, C., Sun, Y., & Piao, L. (2025). The photocatalytic wastewater hydrogen production process with superior performance to the overall water splitting. *Journal of Colloid and Interface Science, 677*, 189–197. [https://doi.org/10.1016/j.jcis.2024.06.039](https://doi.org/10.1016/j.jcis.2024.06.039?utm_source=chatgpt.com)

Haider, H., Azeem, H., Anwar, M., Ali, M. A. S., Khoja, A. H., Hassan, M., Liaquat, R., & Bahadar, A. (2025). Photo- and electrocatalytic hydrogen production from dye-degraded wastewater using samarium-doped ceria as a catalyst. *International Journal of Hydrogen Energy, 111*, 606–622. [https://doi.org/10.1016/j.ijhydene.2025.02.188](https://doi.org/10.1016/j.ijhydene.2025.02.188?utm_source=chatgpt.com)

El-Fawal, E. M., El Naggar, A. M. A., & Zaki, T. (2025). Transformation of dye-contaminated water into renewable hydrogen with in-situ wastewater treatment using a SnS-modified nitrogen-rich Zr-MOF as effective visible-light photocatalyst. *International Journal of Hydrogen Energy*. [https://doi.org/10.1016/j.ijhydene.2025.152302](https://doi.org/10.1016/j.ijhydene.2025.152302?utm_source=chatgpt.com)

Kanwal, H., Khoja, A. H., Hajji, Y., Shakir, S., Anwar, M., Liaquat, R., Din, I. U., Bahadar, A., & Hleili, M. (2025). Photocatalytic performance of dual-function selenium-enriched biomass-derived activated carbon as a catalyst for dye degradation and hydrogen production. *International Journal of Hydrogen Energy, 101*, 1288–1303. [https://doi.org/10.1016/j.ijhydene.2024.12.509](https://doi.org/10.1016/j.ijhydene.2024.12.509?utm_source=chatgpt.com)

Bianchini, P., Profumo, A., Cerri, L., Tedesco, C., Malavasi, L., & Speltini, A. (2025). Exploiting rice industry wastewater for more sustainable sunlight-driven photocatalytic hydrogen production using a graphitic carbon nitride polymorph. *RSC Sustainability, 3*, 1149–1156. [https://doi.org/10.1039/D4SU00567H](https://doi.org/10.1039/D4SU00567H?utm_source=chatgpt.com)

Sau, A., Mondal, D., Roy, J., Bag, N., Ghosh, S., Biswas, D., & Das, S. (2026). Recent advances in piezo-photo heterojunction: A review on dual catalytic function for wastewater remediation and simultaneous hydrogen generation. *Coordination Chemistry Reviews*. [https://doi.org/10.1016/j.ccr.2025.217240](https://doi.org/10.1016/j.ccr.2025.217240?utm_source=chatgpt.com)

E. Additional photocatalytic wastewater and dye degradation literature

Aina, A. R. N., Patel, H., Aich, S., Roy, B., Samanta, N. S., et al. (2025). Recent advances in ZnO based photocatalysts for industrial dye degradation. *Discover Applied Sciences, 7*, 977.

Chauke, N. M., Ngqalakwezi, A., & Raphulu, M. (2025). Transformative advancements in visible-light-activated titanium dioxide for industrial wastewater remediation. *International Journal of Environmental Science and Technology, 22*, 8521–8552. [https://doi.org/10.1007/s13762-025-06397-2](https://doi.org/10.1007/s13762-025-06397-2?utm_source=chatgpt.com)

Samy, M., Tang, S., Zhang, Y., & Leung, D. Y. C. (2024). Understanding the variations in degradation pathways and generated by-products of antibiotics in modified TiO_2 and ZnO photodegradation systems: A comprehensive review. *Journal of Environmental Management*. [https://doi.org/10.1016/j.jenvman.2024.122402](https://doi.org/10.1016/j.jenvman.2024.122402?utm_source=chatgpt.com)

Jari, Y., Najid, N., Necibi, M. C., Gourich, B., Vial, C., Elhalil, A., Kaur, P., Mohdeb, I., Park, Y., Hwang, Y., Ruiz Garcia, A., Roche, N., & El Midaoui, A. (2025). A comprehensive review on TiO_2-based heterogeneous photocatalytic technologies for emerging pollutants removal from water and wastewater: From engineering aspects to modeling approaches. *Journal of Environmental Management, 373*, 123703. [https://doi.org/10.1016/j.jenvman.2024.123703](https://doi.org/10.1016/j.jenvman.2024.123703?utm_source=chatgpt.com)

Abou Zeid, S., & Leprince-Wang, Y. (2024). Advancements in ZnO-based photocatalysts for water treatment: A comprehensive review. *Crystals, 14*(7), 611. [https://doi.org/10.3390/cryst14070611](https://doi.org/10.3390/cryst14070611?utm_source=chatgpt.com)

Iqbal, M. A., Akram, S., Khalid, S., Lal, B., Hassan, S. U., Ashraf, R., & Kezembayeva, G. (2024). Advanced photocatalysis as a viable and sustainable wastewater treatment process: A comprehensive review. *Environmental Research, 253*, 118947. [https://doi.org/10.1016/j.envres.2024.118947](https://doi.org/10.1016/j.envres.2024.118947?utm_source=chatgpt.com)

Rao, A., Thakur, P., & Thakur, A. (2026). Recent advances in photocatalytic degradation for dye-contaminated wastewater: A review on kinetic insights and metal oxide nanoparticle approaches. *Inorganic Chemistry Communications, 188*, 116562. [https://doi.org/10.1016/j.inoche.2026.116562](https://doi.org/10.1016/j.inoche.2026.116562?utm_source=chatgpt.com)

Solihu, L. A., Akinsola, S. I., Alabi, A. B., et al. (2026). A systematic review on photocatalytic activities of metal oxide semiconductors (MOS) for wastewater: Dye degradation. *Applied Water Science, 16*, 292. [https://doi.org/10.1007/s13201-026-02957-0](https://doi.org/10.1007/s13201-026-02957-0?utm_source=chatgpt.com)

Saif, A., Rizvi, S. I., Shaukat, Z., Saif, M., Tabassum, S., Khalid, R., Javed, F., Rebouh, N. Y., Hassan, F., & Zaman, Q. (2025). Development of composite catalyst containing renewable biochar blended with zinc oxide and copper diphenyl amine for visible light photocatalytic degradation of methylene blue. *Frontiers in Sustainable Food Systems, 9*, 1500907. [https://doi.org/10.3389/fsufs.2025.1500907](https://doi.org/10.3389/fsufs.2025.1500907?utm_source=chatgpt.com)

Rana, A., Sonu, S., Soni, V., Chawla, A., Sudhaik, A., Raizada, P., Ahamad, T., Thakur, P., Thakur, S., & Singh, P. (2025). Novel S-scheme derived Mo–Bi_2WO_6/WO_3/biochar composite for photocatalytic removal of methylene blue dye. *Journal of Physics and Chemistry of Solids*, 112385. [https://doi.org/10.1016/j.jpcs.2024.112385](https://doi.org/10.1016/j.jpcs.2024.112385?utm_source=chatgpt.com)

Kandasamy, B., Govindasamy, P., Thangavelu, P., Phibanchon, S., Nakyai, T., Pannaracha, P., Wongcharee, S., Rojviroon, T., & Suwannahong, K. (2026). Circular economy-driven wastewater treatment via rice husk-derived carbon-rich-SiO_2/Bi_2WO_6 nanocomposites: Photocatalytic oxidation efficiency and environmental performance assessment. *Water Cycle*. [https://doi.org/10.1016/j.watcyc.2026.09.002](https://doi.org/10.1016/j.watcyc.2026.09.002?utm_source=chatgpt.com)

Nazeer, N., Mahmood, F., Umar, A., Patel, D. S., Sandeep, V., Kumar, R., Singh, K., Jafarli, M., Smerat, A., & Singh, S. (2026). Sustainable biochar–TiO_2 nanocomposites for efficient photocatalytic degradation of malachite green and rhodamine B in single and binary dye systems. *Surfaces and Interfaces, 95*, 109845. [https://doi.org/10.1016/j.surfin.2026.109845](https://doi.org/10.1016/j.surfin.2026.109845?utm_source=chatgpt.com)

2026 by the authors; Journal of *Kashmir Journal of Academic Research and Development*. This is an open access article distributed under the terms and conditions of the Creative Commons Attribution (CC-BY) license (http://creativecommons.org/licenses/by/4.0/).